Full wavefield least squares reverse time migration

Davydenko, Mikhail; Verschuur, Eric

Publication date
2021

Document Version
Accepted author manuscript

Published in
Geophysics

GEOPHYSICS®

Full Wavefield Least-Squares Reverse Time Migration

Journal:	*Geophysics*
Manuscript ID	GEO-2020-0866.R2
Manuscript Type:	Advances in seismic multiple reflection processing
Keywords:	internal multiples, full-waveform inversion, Reverse time migration, imaging, scattering
Manuscript Focus Area:	Seismic Inversion, Special Section

DOI:10.1190/geo2020-0866.1

DOI: 10.1190/geo2020-0866.1

Full Wavefield Least Squares Reverse Time Migration

Mikhail Davydenko [*], **Eric Verschuur** [†]

[*] *Wavekoda,*

The Hague, The Netherlands

[†] *Delft University of Technology,*

Lorentzweg 1

Delft, 2628 CJ

(June 29, 2021)

GEO-2020-0866

Running head: **Full wavefield LSRTM**

ABSTRACT

Waveform inversion based on least-squares reverse time migration (LSRTM) usually involves Born modeling, which models the primary-only data. As a result the inversion process handles only primaries and corresponding multiple elimination pre-processing of the input data is required prior to imaging and inversion. Otherwise, multiples left in the input data are mapped as false reflectors, also known as crosstalk, in the final image. At the same time the developed full wavefield migration (FWM) methodology can handle internal multiples in an inversion-based imaging process. However, because it is based on the framework of the one-way wave equation, it cannot image dips close to and beyond 90°. Therefore, we aim at upgrading the LSRTM framework by bringing in the functionality of FWM to handle

[**]

[††]

internal multiples. We inject the secondary source term, as used in the original formulation of FWM to define a wavefield relationship that allows to model multiple scattering via reflectivity. The secondary source term is based on the estimated reflectivity and can be injected into the pressure component when simulating the two-way wave equation using finite-difference modeling. We use this modified forward model for estimating the reflectivity model in a FWM-type manner and validate the method on both synthetic and field data containing visible internal multiples.

DOI: 10.1190/geo2020-0865.1

INTRODUCTION

Reverse time migration (RTM) (Baysal et al., 1983; Whitmore, 1983) has become the industry-standard for seismic imaging in complex media over the last two decades. It exploits the discretized wave equation for its forward operator to compute Green's functions. The modeling operator based on the two-way wave equation is very accurate and accounts for many effects that are crucial when imaging a complex subsurface, such as using diving waves and imaging steep structures.

The resolution of seismic images obtained by the RTM method can be further enhanced by applying an inversion-based approach, that is, by using least-squares RTM (LSRTM) (Yao and Jakubowicz, 2012; Wong et al., 2012). The ability to resolve the crosstalk from multiple scattering is another advantage of an inversion-based approach. In this way, it is possible to include multiple scattering in the forward model and handling the crosstalk by fitting the multiply-scattered modeled events with the observed data. Including surface-related multiples is a relatively straightforward approach that requires modifying the source-side wavefield by additional re-injection of the observed data at the receiver locations (Zhang and Schuster, 2013; Zuberi and Alkhalifah, 2013; Wong et al., 2015; Yang and Herrmann, 2017; De Vos, 2020a; Qu et al., 2020a). In contrast, the process of including internal multiples remains difficult. The first obvious way to include internal multiple scattering in the imaging is to use sharp density and velocity models. However, usually these models are not known in high detail and scattering should be based on the estimated reflectivivty or the high-frequency component of the velocity model. Therefore, the LSRTM method uses a de-migration operator to map the estimated reflectivity back into the predicted surface reflection response. However, such a de-migration process based on the Born approxima-

DOI: 10.1190/geo2020-0865.1

tion suggests primaries-only wavefield modeling. Thus, additional effort has to be done to simulate internal multiple scattering from the reflectivity. In literature, there are several methods that include internal multiples in LSRTM. One family of methods accumulates additional orders of scattering by additional modeling (Zuberi and Alkhalifah, 2014; Alkhalifah and Wu, 2016; Guo and Alkhalifah, 2017; Yang et al., 2019; Alkhalifah and Guo, 2019; De Vos, 2020b). Thus, cascading of single scattered modeling iterations add up additional orders of scattering. Such an approach is very robust but modeled scattering orders are finite. Moreover, further modeling iterations bring additional costs. Another approach exploits modifying the wave equation in such a way that it avoids the Born-approximation at all (Wu and Alkhalifah, 2017). Our proposed method has more similarities with the latter method and forms with it a second 'group' of methods that generate multiple scattering not iteratively, but within a single simulation. It is important to mention recent work by Whitmore et al. (2020), belonging to the same second group, that also aims at similar goals as we do in this paper. The difference is in the derivation. The indicated method proposes substitution of the variables in the acoustic wave equation, whereas in this paper we introduce the scattering term from the perspective of Full Wavefield Migration (FWM). Moreover, we consider wavefield modeling via a first-order wave equation based on pressure and particle velocity components.

The original FWM method is based on the one-way wave equation (Berkhout, 2014b) and is thereby limited in its ability to image steep dips or use diving waves. We translate the physics of the secondary source term (Berkhout, 2014a), which is proportional to the wavefield scaled by the local reflectivity. We attempt to re-inject this secondary source during the forward modeling driven by the finite-difference modeling scheme.

In the next section, we will discuss our forward model and subsequently introduce the

inversion-based imaging scheme. Next, we demonstrate the approach using numerical and field data.

THEORY

We consider the acoustic two-way wave equation as a system of first-order partial differential equations (PDE) written in an operator form:

$$\mathcal{L}(\rho, c)\mathbf{u} = \mathbf{s}, \tag{1}$$

where $\mathbf{s}$ is a source vector, vector $\mathbf{u}$ includes wavefield components:

$$\mathbf{u} = \begin{pmatrix} p \\ v_x \\ v_z \end{pmatrix}, \tag{2}$$

such as pressure $p(\mathbf{x})$, horizontal $v_x(\mathbf{x})$ and vertical $v_z(\mathbf{x})$ particle velocity components, respectively, (vector $\mathbf{x}$ defines spatial location). Finally, $\mathcal{L}$ is a differential operator, given by:

$$\mathcal{L}(\rho, c) = \begin{pmatrix} \partial_t & -\rho c^2 \partial_x & -\rho c^2 \partial_z \\ \frac{1}{\rho}\partial_x & \partial_t & 0 \\ \frac{1}{\rho}\partial_z & 0 & \partial_t \end{pmatrix}. \tag{3}$$

The operator $\mathcal{L}$ contains spatial and time partial derivatives ∂_* as well as spatially variable density $\rho(\mathbf{x})$ and velocity $c(\mathbf{x})$ models.

In this paper we compare two reflectivity-based modeling approaches. The first approach is based on the single-scattering assumption and is also known as the Born approximation. The second modeling approach is based on the full-wavefield modeling approach (Berkhout,

2014a) and, thereby, it operates beyond the Born approximation. Before conducting numerical experiments, we first discuss these approaches in more details.

Single-scattering modeling

Following Zhang et al. (2015) and translating this approach to the first-order wave equation, we obtain the single-scattering modeling based on the Born approximation:

$$\mathcal{L}(c_m, \rho_0)\delta\mathbf{u} = \delta\mathbf{s}_0, \tag{4}$$

where c_m is the migration velocity model, ρ_0 is the homogeneous density model and $\delta\mathbf{s_0}$ is:

$$\delta\mathbf{s}_0 = \mathcal{R}\mathbf{u} = \begin{pmatrix} r & 0 & 0 \\ 0 & 0 & 0 \\ 0 & 0 & 0 \end{pmatrix} \begin{pmatrix} p \\ v_x \\ v_z \end{pmatrix}, \tag{5}$$

with $\mathbf{u}$ being a wavefield modeled using equation 1 (modeled also by using a homogeneous density model ρ_0 and a migration velicity model c_m). Therefore, to compute the modeled wavefield using the Born approximation, it is required to compute the background wavefield $\mathbf{u}$, that is then involved in the right-hand side of equation 4 of the second modeling experiment. This two-step process produces the scattered wavefield. It is important to mention that in this case the wavefield is modeled under a single-scattering assumption and, hence, can simulate primary reflections only. To overcome this assumption and to compute two-way wavefields using reflectivity beyond the Born approximation, we use a full-wavefield formulation as discussed in the next subsection.

Full wavefield modeling

To include multiple scattering in a two-way wave equation we refer to the theory of full wavefield migration (FWM) originally derived in the context of the one-way wave equation (Berkhout, 2014b). Figure 1 demonstrates the principle of FWM – the theory considers wavefields propagating in the downward and upward directions and as these wavefields propagate only either upward or downward, the scatterring is not generated without explicit use of the scattering operator δs. The application of the scattering operator is also necessary to fulfill the continuity of the wavefield at each boundary. Considering that every gridpoint in the subsurface is illuminated by the incoming downgoing p^+ and upgoing p^- wavefields, these wavefields are potentially transmitted and reflected, depending on the value of the reflectivity at this point. Thereby, the total scattered downgoing $q+$ and upgoing $q-$ are scattered wavefields that leave the gridpoint. It is the scattering term δs that is responsible for the scattering, which allows the wavefield to change its direction to be dependent on the transmission coefficients.

$$\delta s = r^+ p^+ + r^- p^-, \tag{6}$$

To include the scattering term in a two-way wave equation, we need to avoid requiring the downgoing and upgoing wavefields and operate with the omnidirectional wavefield $\mathbf{u}$. We replace these one-way wavefields (p^+ and p^-) with the wavefield decomposition equation:

$$p^\pm = \frac{1}{2}(p \pm \frac{\rho c^2}{cos\theta} v_z). \tag{7}$$

By substituting equation 7 into equation 6, and assuming the acoustic approximation ($r^- = -r^+$) we can derive a scattering term suitable for the two-way wave equation:

$$\delta s = r^{+} \frac{\rho c^2}{cos\theta} v_z. \tag{8}$$

Next, we inject this scattering term as a source function in equation 1 and translate this term to the left hand side, which allows us to derive a modified wave equation operator as follows:

$$\mathbf{L}_1(c, \rho, r) = \begin{pmatrix} \partial_t & -\rho c^2 \partial_x & -(\rho c^2 \partial_z + r \frac{\rho c^2}{cos\theta}) \\ \frac{1}{\rho}\partial_x & \partial_t & 0 \\ \frac{1}{\rho}\partial_z & 0 & \partial_t \end{pmatrix}. \tag{9}$$

The main feature of using the forward modeling based on equation 9 is that it allows us to simulate the full wavefield using the reflectivity and a background velocity model. To exclude the scattering from the velocity model we might need to use smooth velocity model and homogeneous density models, thereby using $\mathbf{L}(c_m, \rho_0)$ operator. Additional measures can be taken by introducing extra terms in the wave-equation (Baysal et al., 1984).

The main advantage of the discussed modeling scheme is that the modeled wavefield is computed within only one simulation, without first computing the incident wavefield first and then the scattered wavefield as a next step.

Modeling example

We demonstrate an example of the proposed forward modeling and compare it with standard forward modeling, where only the model contrasts cause scattering. While the velocity model, shown in Figure 2a, is homogeneous (1500 m/s), the density model includes a layer with a strong enough contrast to generate visible higher-order scattering (see Figure 2b). The corresponding reflectivity model is displayed in Figure 2c. The grid sampling of the

model is 5m. To model the data a 20 Hz Ricker wavelet was used and injected at the surface at the central location (x=250 m).

While performing modeling experiments with the conventional wave-equation in Figure 3a, we see a snapshot of the modeled wavefield initiated at the central lateral location at the surface. The simulated wavefield contains multiple reflections. At the same time, if we put the density homogeneous and the modeling experiment is driven by the wave equation involving the Born approximation, and the reflectivity controls the scattering, only primary reflections are generated (Figure 3b). After that, we run a simulation with the proposed modified wave equation and now we successfully simulate the full wavefield using only a reflectivity model, while the density is still homogeneous. The resulting wavefield is shown in Figure 3c. Note the strong resemblance with the result shown in Figure 3a.

About the computational cost of the three modeling experiments we can mention the following. The finite difference modeling of the two-way wave equation (shown in Figures 3a and 4a) requires one forward pass in time. The simulation based on the Born approximation, shown in Figures 3b and 4b, requires two simulations: computing the background modeled wavefield and, next, computing the scattered wavefield. The proposed full-wavefield modeling scheme (shown in Figures 3c and 4c) produces all orders of scattering simultaneously. Thus, it also requires only a single forward modeling pass.

INVERSION

For the inversion process, we minimize the data residual between the observed data $\mathbf{u}_{obs}$ and the modeled data $\mathbf{u}$:

$$\Delta\mathbf{u} = \mathcal{P}\mathbf{u} - \mathbf{u}_{obs}, \tag{10}$$

where $\mathcal{P}$ is a picking operator that selects wavefield at the detector locations and selects available wavefield components. The objective function can be defined as follows:

$$J(r) = \|\Delta \mathbf{u}\|_2^2 \rightarrow min. \tag{11}$$

Hence, the process of deriving the gradient for the proposed method is not different from deriving a gradient for conventional LSRTM or FWI. Differentiation of the objective function with the respect to the model (reflectivity in our case) gives:

$$\frac{\partial J}{\partial r} = \sum_{shots} \langle [\frac{\partial \mathbf{u}(r)}{\partial r}]^*, \mathcal{P}^* \Delta u \rangle. \tag{12}$$

The difference with a standard LSRTM is in the wavefield modeling process and computing the derivative of the wavefield with the respect to the model.

For the case of the single-scattering modeling (conventional LSRTM), we differentiate both sides of equation 4 with the respect to the reflectivity and obtain the following expression:

$$\frac{\partial \mathbf{u}}{\partial r} = \mathcal{L}^{-1} \delta \mathbf{u}. \tag{13}$$

Substituting equation 13 into equation 12 we may interpet the gradient as a cross-correlation of the re-injected and back-propagated residuals with the forward modeled wavefield.

In case of full-wavefield modeling, operator $\mathcal{L}(r)$ is dependent on the reflectivity as well. Therefore, differentiation of both sides of equation 9 with respect to the reflectivity gives the following expression:

$$\frac{\partial \mathbf{u}}{\partial r} = \mathcal{L}^{-1} \frac{\partial \mathcal{L}}{\partial r} \mathbf{u}. \tag{14}$$

By substituting equation 14 into equation 12 we can interpret this similar to before as injecting and back-propagating a residual wavefield, however due to the $\frac{\partial \mathcal{L}}{\partial r}$ term, now the

pressure component of the back-propagated residual wavefield should be cross-correlated with the forward modeled v_z component.

After deriving the gradients, we apply the same steepest descent algorithm for both single-scattering and full-wavefield approaches. We update the reflectivity at iteration i as follows:

$$r_i = r_{i-1} + \alpha \frac{\partial J}{\partial r}, \tag{15}$$

where α is an optimal step length.

Extended imaging

We can also extend the method to handle subsurface offset domain common image gathers (ODCIGs) (Sava and Vasconcelos, 2011). ODCIGs are very useful for extending the reflectivity model such that the residual can be minimized efficiently, even when using an erroneous velocity model (Symes, 2017). Therefore, we can relax the sensitivity of the reflectivity for velocity error and still explain the data. Nevertheless, the extended reflectivity can still be sensitive to velocity errors. Evaluating the accuracy of the migration velocity model can be done by measuring the focusing of these gathers across the zero subsurface offset.

The extended imaging condition can be expressed as follows:

$$r(x, z, h) = \sum_t p_s(x + h, z, t) p_r(x - h, z, t), \tag{16}$$

where p_r and p_s are general receiver-side and source-side wavefields respectively.

For modeling, we can use the extended reflectivity and inject the secondary source term

as follows:

$$\delta s(x,z,t) = \frac{\rho_0 c_0^2}{cos\theta} \sum_h r(x-h,z,t) p_s(x-2h,z,t). \tag{17}$$

In this case, we can generate internal multiples and transmission effects accurately, similar to the one-way wave equation based implementation (Davydenko and Verschuur, 2019).

EXAMPLES

In this section, we demonstrate a set of synthetic examples and conclude this section by a field data example from the Vøring basin. In the synthetic example, we set strong contrasts to the density model to emphasize the strength of crosstalk from internal multiples. It is important to note that the method is not limited to density contrasts. Moreover, we also demonstrate extended imaging that is known for handling strong velocity contrasts.

Horizontally layered model

We begin the modeling examples first with the earlier discussed simple horizontally layered model where the velocity model is homogeneous (Figure 2a), the contrast is present in the density model displayed in Figure 2b. The numerical experiment has the following setup: grid spacing of the model is 5m, receiver spacing is 10m, shot spacing is 50m, maximum frequency is 30Hz, and a Ricker wavelet with central frequency 15Hz is used.

Conventional LSRTM based on the Born approximation results in the image with crosstalk from internal multiples (see Figure 5a), whereas the image estimated by FWRTM has suppressed multiple crosstalk, as visible in Figure 5b.

As was mentioned in the inversion section, the method also handles image extension.

DOI: 10.1190/geo2020-0865.1

We use ODCIGs as an image extension. The model remains the same as in the previous example in Figure 5. However, we now create images corresponding to extended imaging and modeling. Figure 6a and 6b show the zero subsurface-offset image and the ODCIG at the central lateral location. Note that both images contain crosstalk. At the same time, the corresponding FWRTM images (Figure 6) have the aforementioned artifacts suppressed. The extended reflectivity was computed using equation 16, whereas modeling was performed based on equation 17.

Figure 7 shows the convergence for the LSRTM and FWRTM methods both in structural and extended modes. Note that the full wavefield approach has better convergence properties. It is also visible that the extended approach has a better opportunity to fit the data. Although for the case of an angle-independent reflection, due to the density contrasts, the non-extended FWRTM finally has the best fit.

Salt structure model

The next example is based on a model that is more typical for demonstrating the potential of RTM methods. The numerical experiment has the following setup: grid spacing of the model is 5 m, receiver spacing is 10 m, shot spacing is 50 m, maximum frequency is 30 Hz, and a 15 Hz Ricker wavelet is used. Now, the velocity model (Figure 8a) includes a vertical velocity gradient, and the density model (Figure 8b) contains not only horizontal layers that generate strong internal multiples but also a salt-like structure with steep flanks. In such a model, the vertical velocity gradient creates diving or refracted waves that can be used for imaging of vertical structures represented in the density model.

We compare the conventional LSRTM with the proposed FWRTM method. Figure 9a

DOI: 10.1190/geo2020-0865.1

shows the LSTRM image, including artifacts and Figure 9b shows the FWRTM image with significantly reduced crosstalk associated with interbed multiples (see the arrows).

Field data

We conclude this section with field data. The data are courtesy of Equinor and originate from the Vøring basin. Due to the approximate 1250 m water depth, surface multiples have no impact on the top 3 km of the image. The measured data have the following sampling: receiver spacing = 25 m, shot spacing = 50 m, time sampling = 8 ms and a maximum frequency of 30 Hz. The original velocity model with a grid spacing of 25 m and 10 m was interpolated to a finer grid of spacing 7 m in both directions to fulfill the finite-difference modeling requirements to avoid modeling dispersion artifacts. This dataset is known for containing strong internal multiples, and was already used for several imaging algorithms with capabilities to handle interbed multiple scattering (Davydenko and Verschuur, 2018; Zhang and Slob, 2020).

We compare the LSRTM algorithm versus the FWRTM approach. As expected, the image of the former method (Figure 10a) contains the crosstalk from internal multiples (indicated by arrows), which is mainly noted in the range of depth levels corresponding to the target area (2200m). In general, the crosstalk in the area overall is recognized by more horizontal dips than the actual dipping reflectors, and the strong presence of this crosstalk significantly complicates interpretation. When examining the image produced by FWRTM (Figure 10b), we observe effective artifact suppression, and the geological fault block structures look more consistent.

Besides crosstalk suppression, evidence of correct handling of internal multiple scat-

tering is demonstrated by the modeled snapshot shown in Figure 11. Given the smooth provided smooth migration velocity model, the scattering generation is only possible via the reflectivity estimated in Figure 10b. Additionally, we show the convergence plot for both methods in Figure 12. Again, it is observed that the full wavefield approach has better convergence properties.

DISCUSSION

The method is still in the development phase and is based on several assumptions. Currently, we include scattering via the vertical particle velocity component, as discussed in equation 6. However, the scattering originating in the near-horizontal direction might also be similarly included using the horizontal particle velocity component and reflectivity. This option will be investigated in the future, especially after extending the method to 3D.

We assume that the scattering originates from the reflectivity and scattering from the velocity and density model is omitted by considering smooth density and smooth background velocity models. Nevertheless, it is interesting to investigate inversion together with sharp velocity variations and how this affects reflectivity estimation. To this end, also terms from non-reflecting wave equations can be included (Baysal et al., 1984).

As with any another method, our approach has its advantages and disadvantages. An advantage of the method is that it allows to image data directly after acquisition as a fast track solution, thereby drastically decreasing the turnaround time to obtain an image. Nevertheless the inversion process can fail and there is no guarantee we can always avoid local minima, which can result in residual crosstalks in the image. It is also expected that model-domain full wavefield reflectivity inversion methods can also get stuck in local minima

in extreme cases such as resonant models where internal multiples can overlap and even cancel some primary events. In such scenarios data-domain internal multiple elimination approaches (Weglein et al., 1997; Zhang and Slob, 2020) can have advantages in resolving internal multiples.

Currently, we are extending the method towards velocity model estimation, which could be done in a reflection waveform inversion (R-FWI) manner (Yao et al., 2020), or using the one-way wave equation analogue to JMI (Berkhout, 2014c).

Like any LSRTM method, the proposed method can also maintain modeling extensions, such as including anisotropy and attenuation (Qu et al., 2020b; Li et al., 2020).

CONCLUSIONS

We have presented a method that models the full wavefield from the (estimated) reflectivity model by using a two-way wave equation and a smooth velocity model. The modeling creates all scattering orders within one computation and, thereby, does not rely on cascading Born modeling iteration steps. Next, we demonstrated that by using this method as a forward model for reflectivity waveform inversion, images appear much cleaner and have suppressed crosstalk from internal multiples, unlike the output of conventional LSRTM. We show that the proposed method can handle interbed multiples similarly in the extended image gathers. The inversion method showed accurate imaging results for synthetic examples and one field data example from the North Sea.

DOI:10.1190/geo2020-0986.1

ACKNOWLEDGMENTS

The authors would like to thank partners of the Delphi Consortium for support and Equinor for the provided field dataset.

REFERENCES

Alkhalifah, T., and Q. Guo, 2019, Subsurface wavefields based on the generalized internal multiple imaging: Geophysical Journal International, **219**, 1212–1224.

Alkhalifah, T., and Z. Wu, 2016, Multiscattering inversion for low-model wavenumbers: Geophysics, **81**, R417–R428.

Baysal, E., D. D. Kosloff, and J. Sherwood, 1984, A two-way nonreflecting wave equation: Geophysics, **49**, 132–141.

Baysal, E., D. D. Kosloff, and J. W. Sherwood, 1983, Reverse time migration: Geophysics, **48**, 1514–1524.

Berkhout, A. J., 2014a, Review paper: An outlook on the future of seismic imaging, part I: forward and reverse modelling: Geophysical Prospecting, **62**, 911–930.

———, 2014b, Review paper: An outlook on the future of seismic imaging, part II: Full-wavefield migration: Geophysical Prospecting, **62**, 931–949.

———, 2014c, Review paper: An outlook on the future of seismic imaging, part III: Joint migration inversion: Geophysical Prospecting, **62**, 950–971.

Davydenko, M., and D. Verschuur, 2018, Including and using internal multiples in closed-loop imaging–field data examples: Geophysics, **83**, 1–36.

———, 2019, Joint imaging of angle-dependent reflectivity and estimation of the migration velocity model using multiple scattering: Geophysics, **84**, R859–R868.

De Vos, K., 2020a, Imaging with multiples: using surface multiples in least squares RTM: , 1–5.

———, 2020b, Internal multiple prediction using reflectivity from least squares RTM with surface multiples: , 1–3.

Guo, Q., and T. Alkhalifah, 2017, Elastic reflection-based waveform inversion with a non-

linear approach: Geophysics, **82**, R309–R321.

Li, Z., Z. Li, Q. Li, Q. Li, M. Sun, P. Hu, and L. Li, 2020, Least-squares reverse time migration of multiples in viscoacoustic media: Geophysics, **85**, S285–S297.

Qu, Y., C. Huang, C. Liu, and Z. Li, 2020a, Full-path compensated least-squares reverse time migration of joint primaries and different-order multiples for deep-marine environment: IEEE Transactions on Geoscience and Remote Sensing.

Qu, Y., J. Li, Z. Guan, and Z. Li, 2020b, Viscoacoustic reverse time migration of joint primaries and different-order multiples: Geophysics, **85**, S71–S87.

Sava, P., and I. Vasconcelos, 2011, Extended imaging conditions for wave-equation migration: Geophysical Prospecting, **59**, 35–55.

Symes, B., 2017, Extended waveform inversion: 79th EAGE Conference and Exhibition 2017-Workshops.

Weglein, A. B., F. A. Gasparotto, P. M. Carvalho, and R. H. Stolt, 1997, An inverse-scattering series method for attenuating multiples in seismic reflection data: Geophysics, **62**, 1975–1989.

Whitmore, N., J. Ramos-Martinez, Y. Yang, and A. Valenciano, 2020, Seismic modeling with vector reflectivity, *in* SEG Technical Program Expanded Abstracts 2020: Society of Exploration Geophysicists, 2709–2713.

Whitmore, N. e. a., 1983, Iterative depth migration by backward time propagation: Presented at the 1983 SEG Annual Meeting, Society of Exploration Geophysicists.

Wong, M., B. Biondi, S. Ronen, and U. Stanford, 2012, Imaging with multiples using linearized full-wave inversion: Society of Exploration Geophysicists, 1–5.

Wong, M., B. L. Biondi, and S. Ronen, 2015, Imaging with primaries and free-surface multiples by joint least-squares reverse time migration: Geophysics, **80**, S223–S235.

Wu, Z., and T. Alkhalifah, 2017, Efficient scattering-angle enrichment for a nonlinear inversion of the background and perturbations components of a velocity model: Geophysical Journal International, **210**, 1981–1992.

Yang, J., Y. Liu, Y. E. Li, A. Cheng, L. Dong, and Y. Du, 2019, Joint least-squares reverse time migration of primary and prismatic waves. lsrtm of prismatic waves: Geophysics, **84**, S29–S40.

Yang, M., and F. J. Herrmann, 2017, Time domain sparsity promoting LSRTM with surface-related multiples in shallow-water case: Presented at the . ((SEG Workshop, Houston)).

Yao, G., and H. Jakubowicz, 2012, Least-Squares Reverse-Time Migration: SEG Las Vegas 2012 Annual Meeting, 1–5.

Yao, G., D. Wu, and S.-X. Wang, 2020, A review on reflection-waveform inversion: Petroleum Science, 1–18.

Zhang, D., and G. T. Schuster, 2013, Least-squares reverse time migration of multiples: Geophysics, **79**, S11–S21.

Zhang, L., and E. Slob, 2020, A field data example of marchenko multiple elimination: Geophysics, **85**, S65–S70.

Zhang, Y., L. Duan, and Y. Xie, 2015, A stable and practical implementation of least-squares reverse time migration: Geophysics, **80**, V23–V31.

Zuberi, A., and T. Alkhalifah, 2013, Imaging by forward propagating the data: Theory and application: Geophysical Prospecting, **61**, 248–267.

Zuberi, M., and T. Alkhalifah, 2014, Generalized internal multiple imaging (GIMI) using feynman-like diagrams: Geophysical Journal International, **197**, 1582–1592.

LIST OF FIGURES

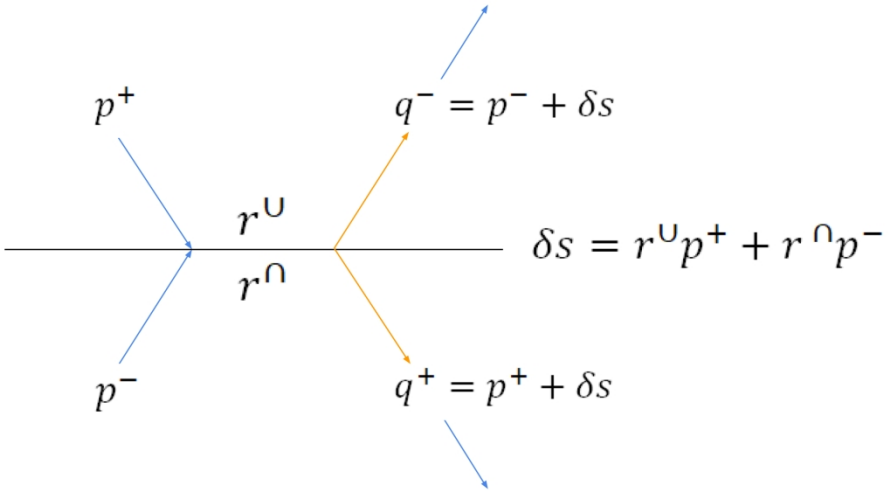

Figure 1

881x562mm (72 x 72 DPI)

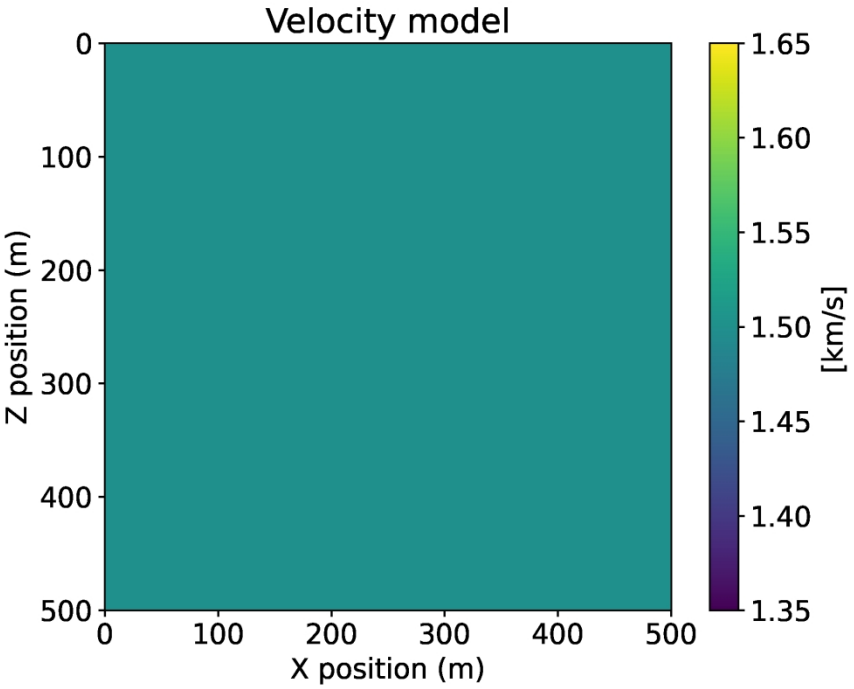

Figure 2a

516x387mm (118 x 118 DPI)

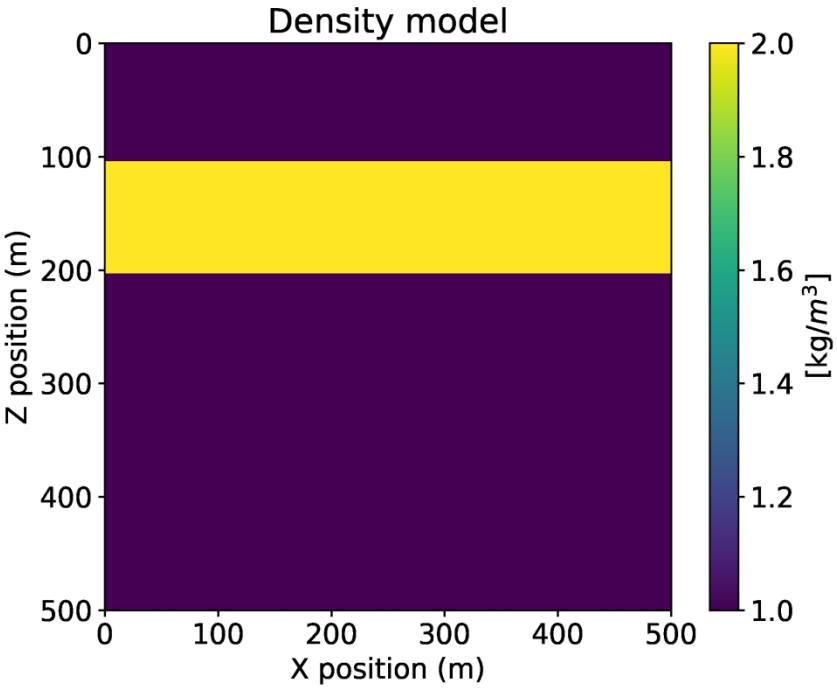

Figure 2b

516x387mm (118 x 118 DPI)

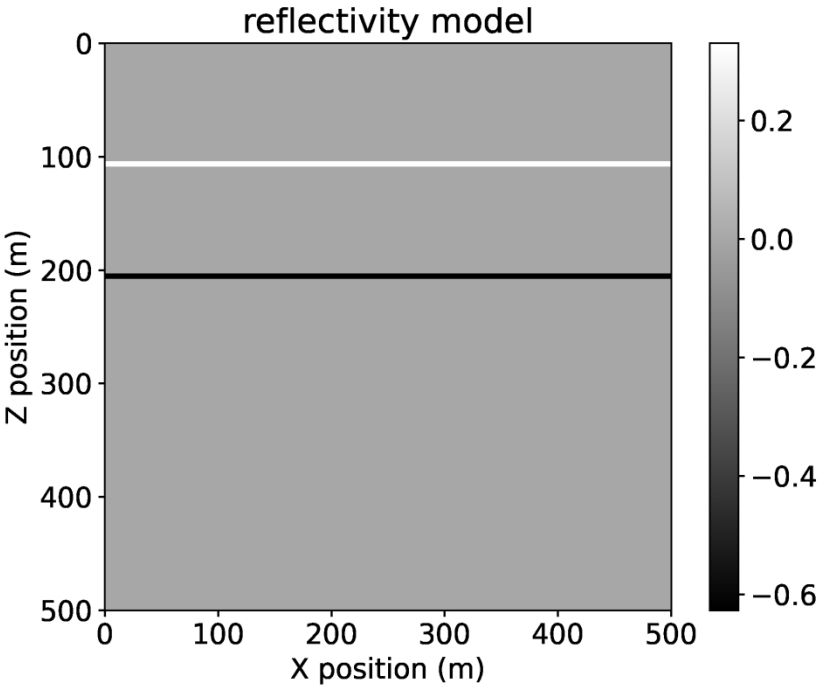

Figure 2c

516x387mm (118 x 118 DPI)

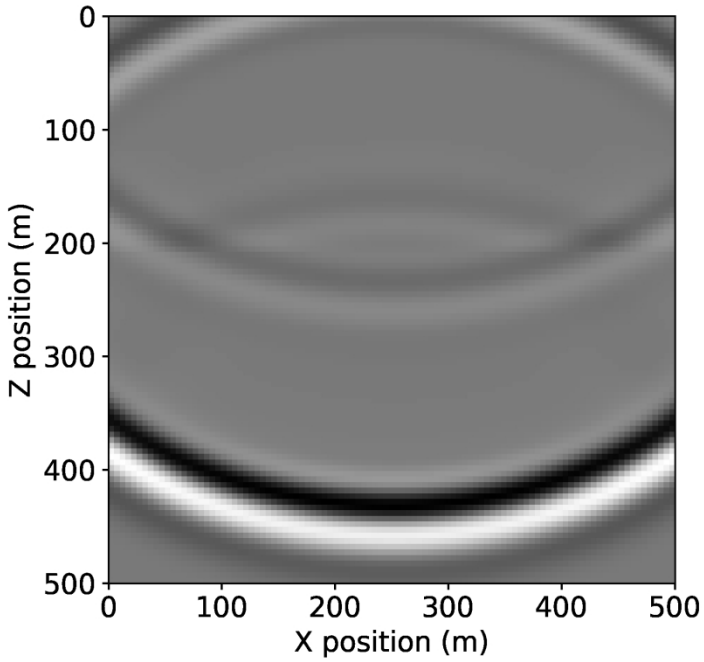

Figure 3a

516x387mm (118 x 118 DPI)

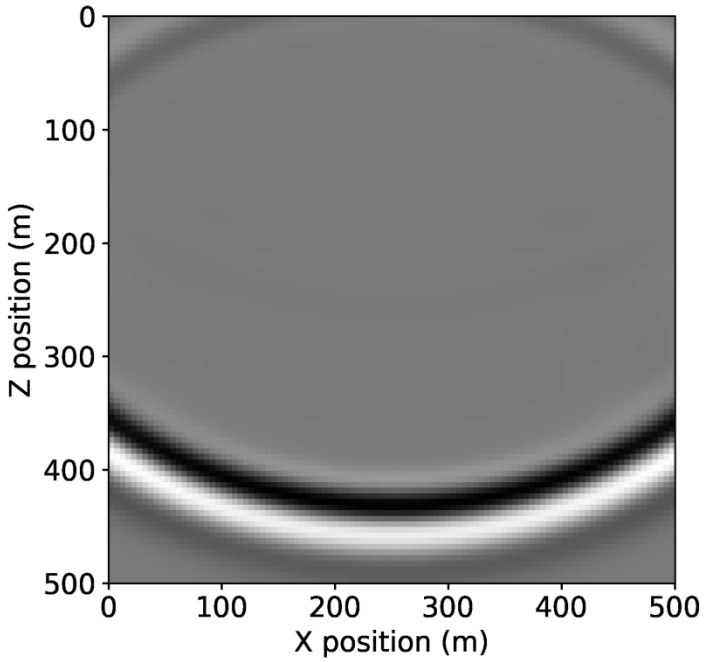

Figure 3b

516x387mm (118 x 118 DPI)

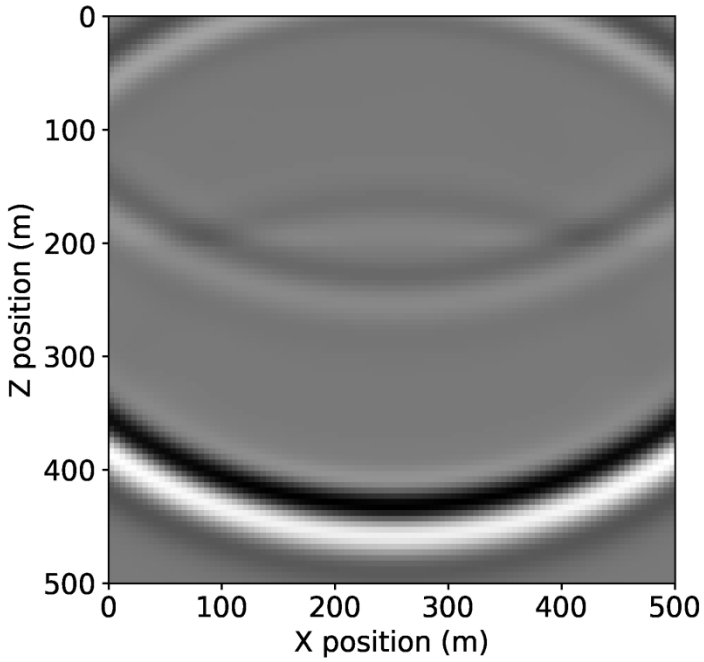

Figure 3c

516x387mm (118 x 118 DPI)

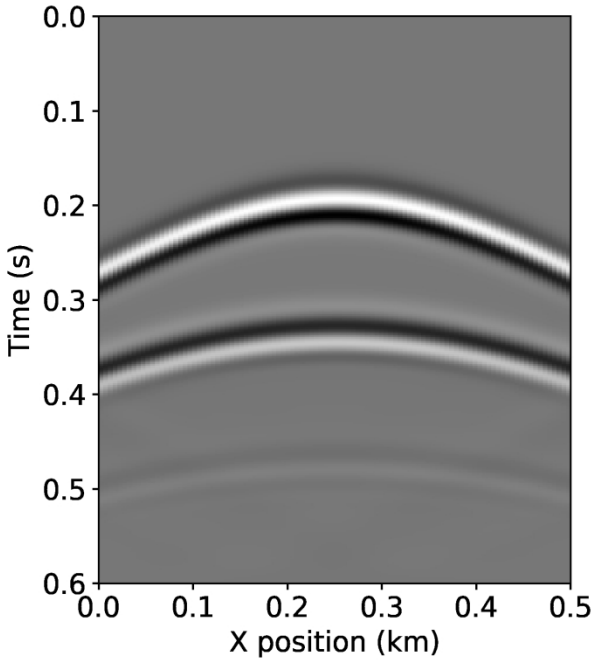

Figure 4a

516x387mm (118 x 118 DPI)

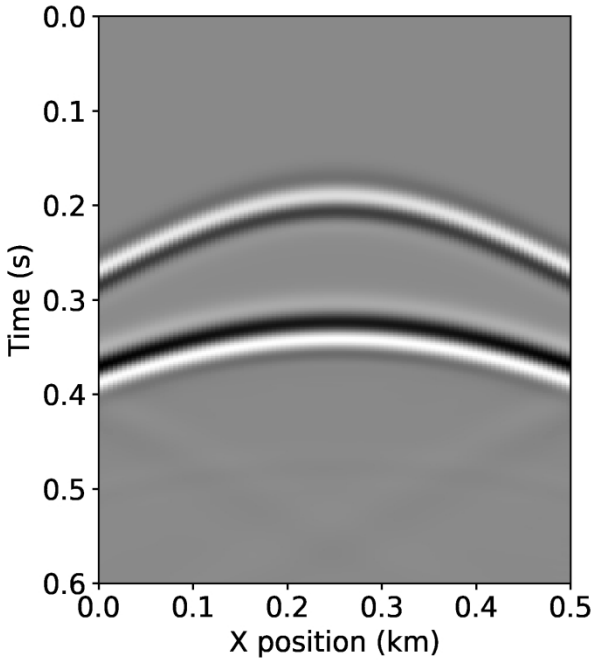

Figure 4b

516x387mm (118 x 118 DPI)

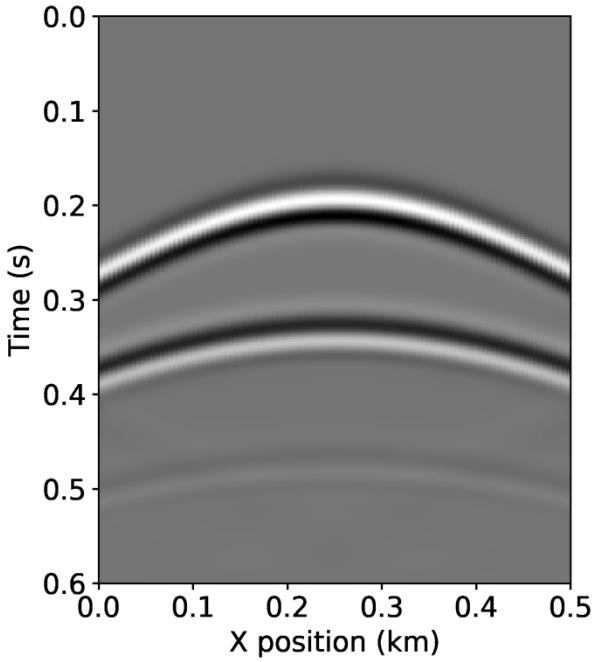

Figure 4c

516x387mm (118 x 118 DPI)

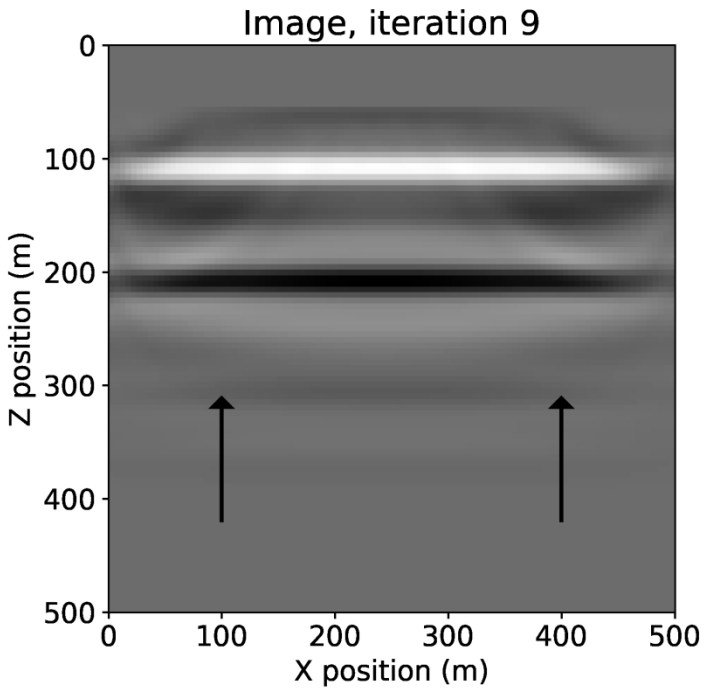

Figure 5a

516x387mm (118 x 118 DPI)

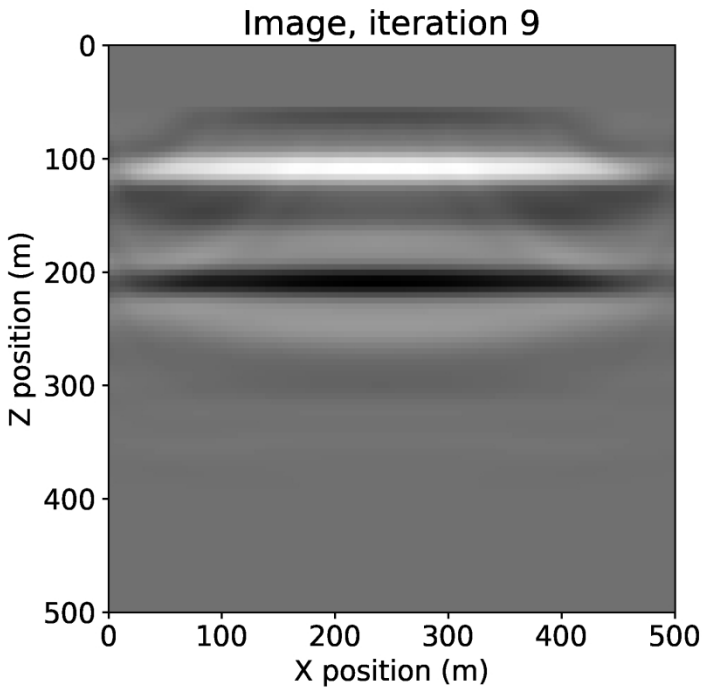

Figure 5b

516x387mm (118 x 118 DPI)

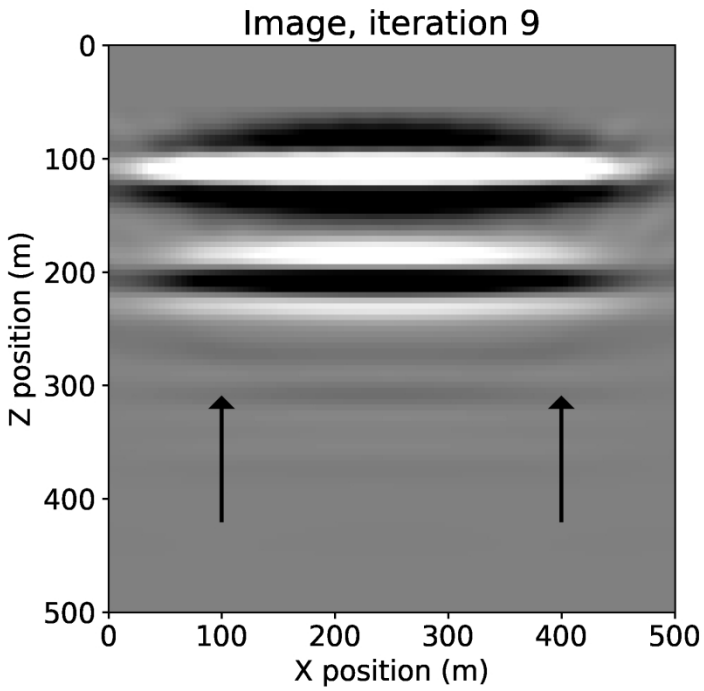

Figure 6a

516x387mm (118 x 118 DPI)

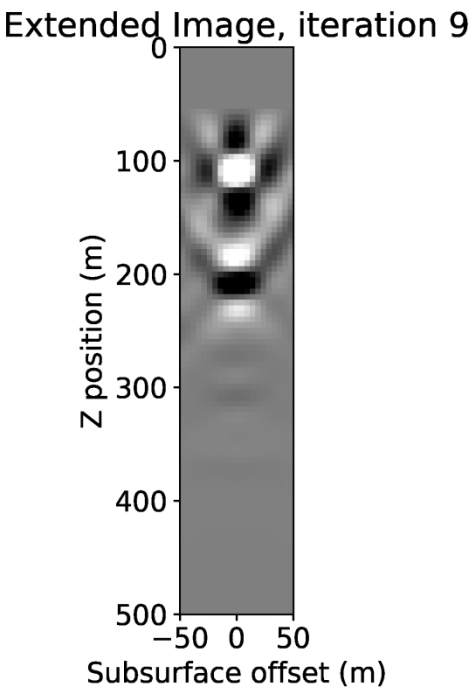

Figure 6b

516x387mm (118 x 118 DPI)

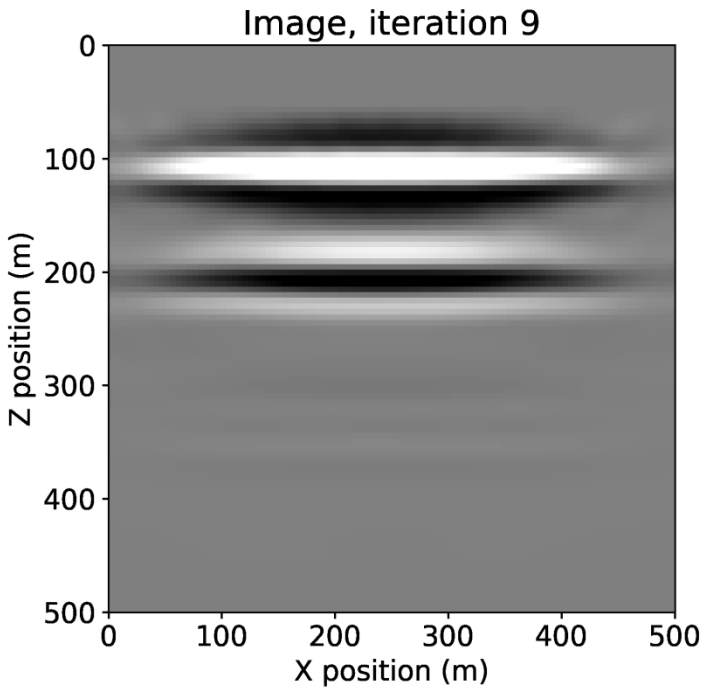

Figure 6c

516x387mm (118 x 118 DPI)

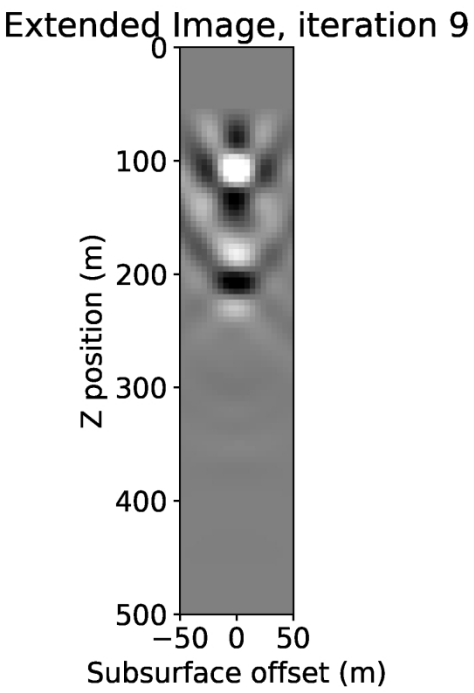

Figure 6d

516x387mm (118 x 118 DPI)

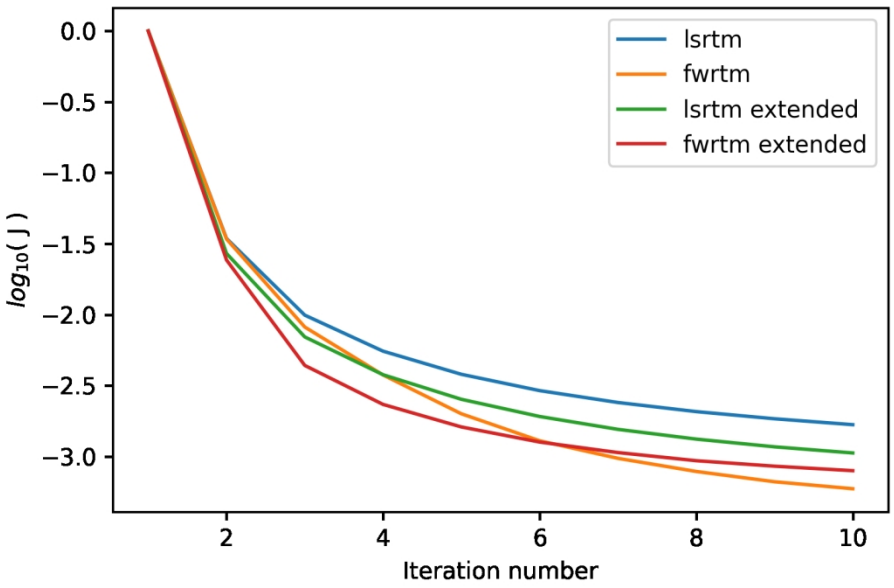

Figure 7

387x258mm (118 x 118 DPI)

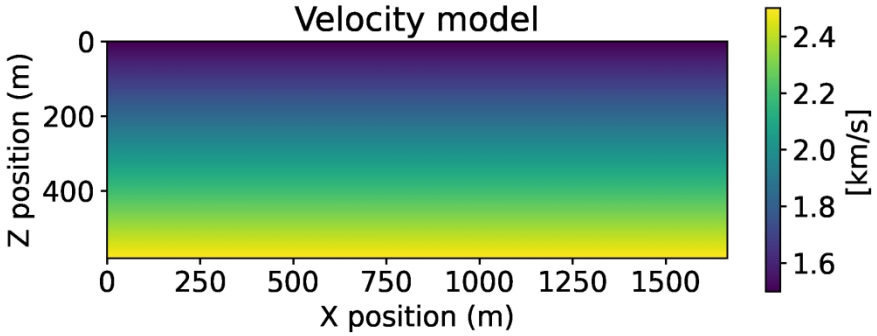

Figure 8a

516x387mm (118 x 118 DPI)

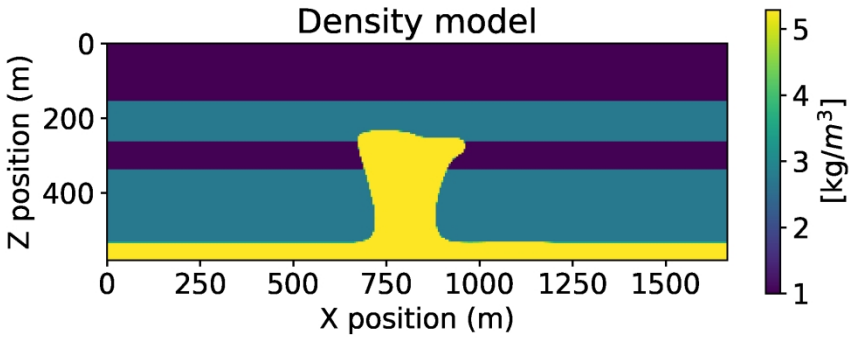

Figure 8b

516x387mm (118 x 118 DPI)

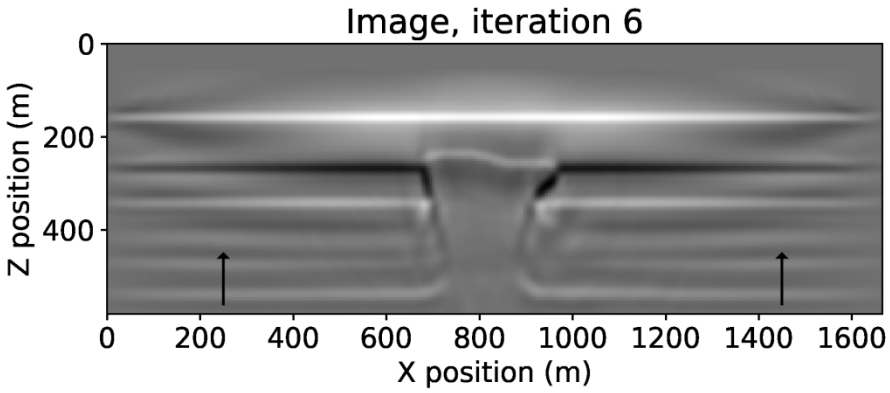

FIgure 9a

516x387mm (118 x 118 DPI)

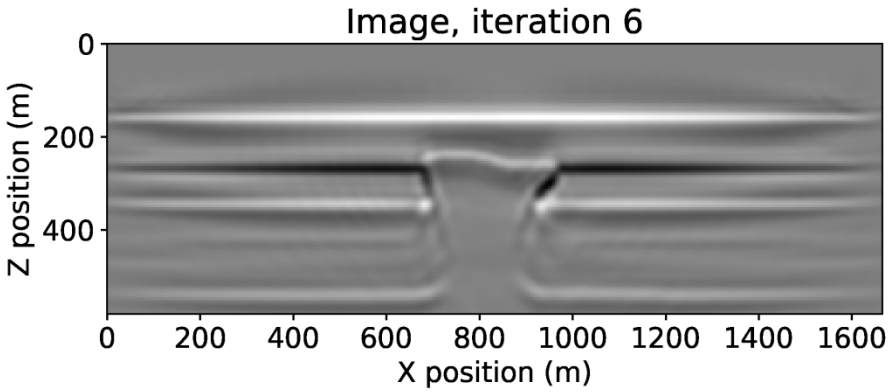

Figure 9b

516x387mm (118 x 118 DPI)

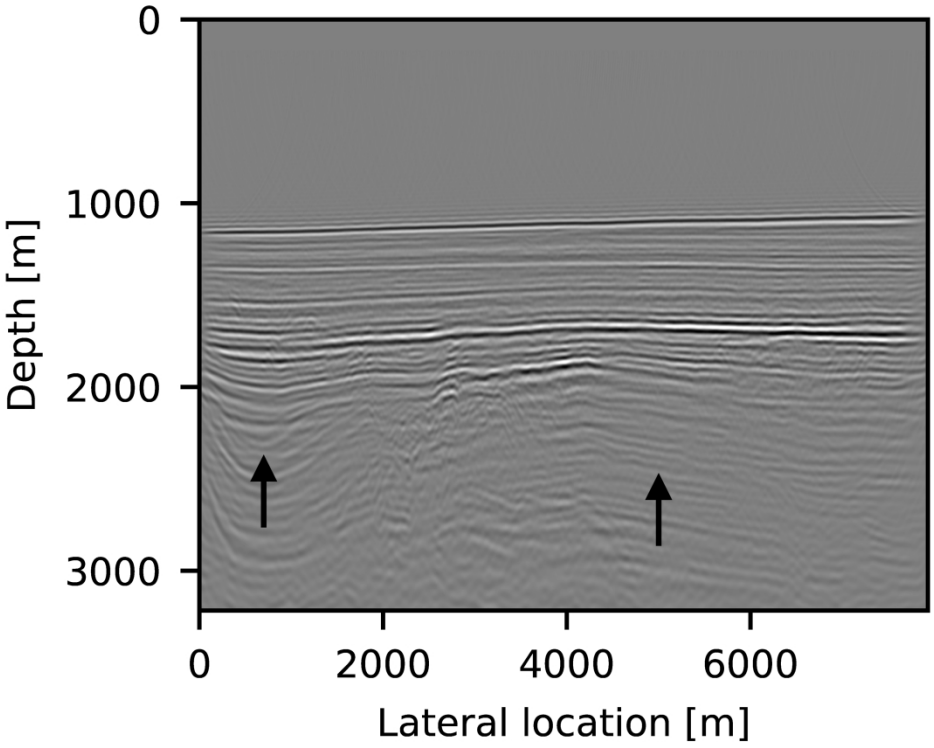

Figure 10a

164x134mm (600 x 600 DPI)

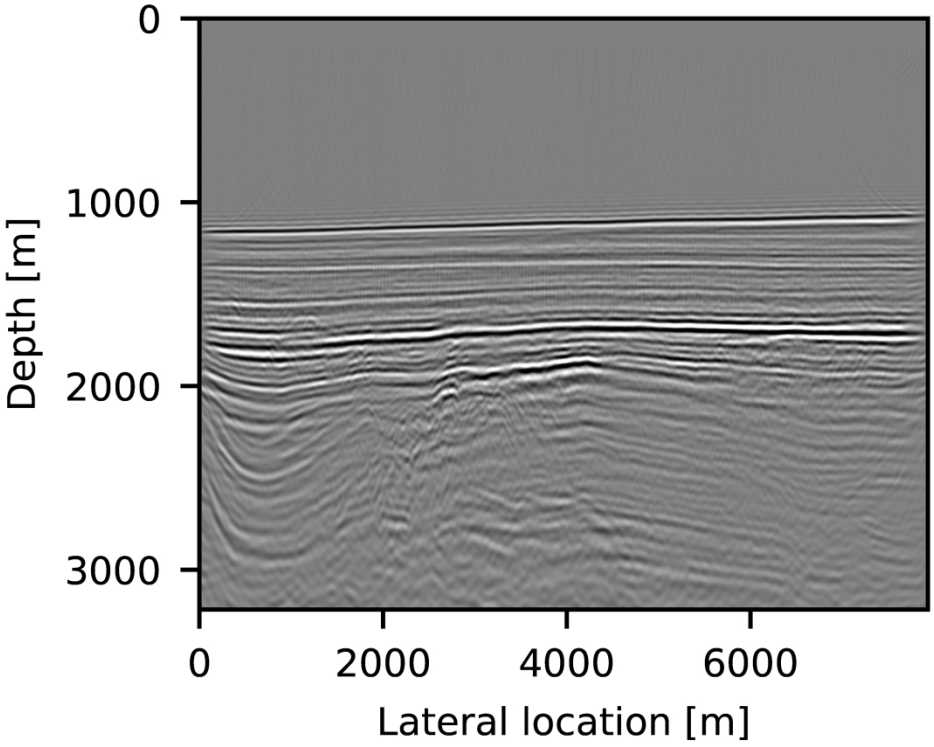

Figure10b

164x134mm (600 x 600 DPI)

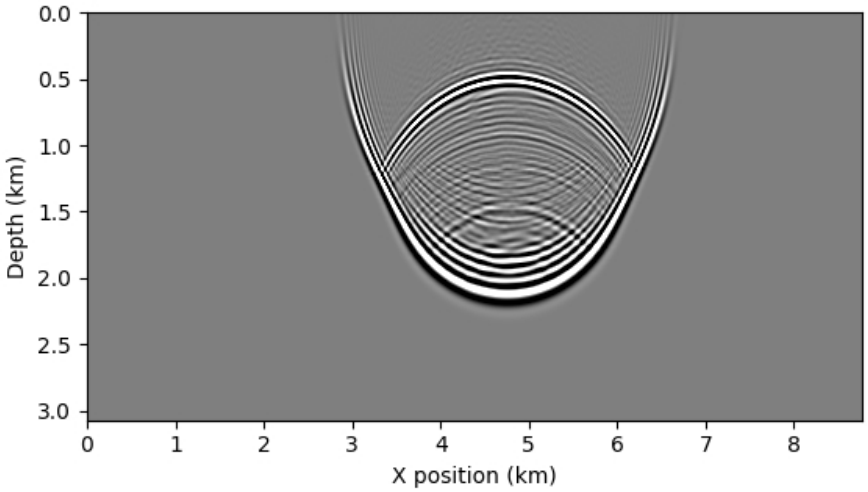

Figure 11

416x312mm (39 x 39 DPI)

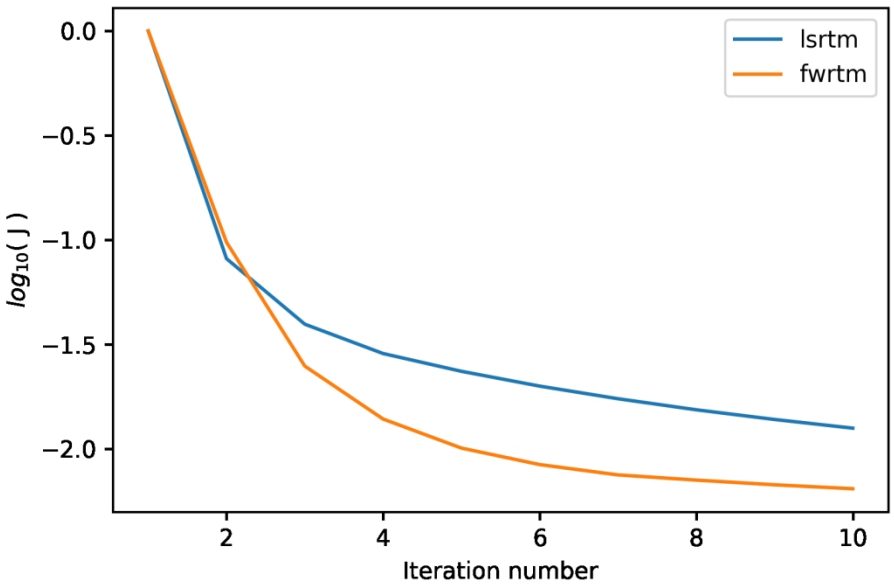

Figure 12

387x258mm (118 x 118 DPI)

DATA AND MATERIALS AVAILABILITY

Custom statement of data and materials availability

DOI:10.1190/geo2020-0866.1